



# Design and mechanistic study of advanced cobalt-based nanostructured catalysts for electrochemical carbon dioxide reduction

Sharon Abner, Aicheng Chen<sup>\*,1</sup>

Electrochemical Technology Centre, Department of Chemistry, University of Guelph, 50 Stone Road East, Guelph, Ontario N1G 2W1, Canada

## ARTICLE INFO

**Keywords:**  
Electrocatalysis  
CO<sub>2</sub> reduction  
Cobalt  
Nanodendrites  
in situ FTIR

## ABSTRACT

The advancement of cost-effective nanostructured catalysts for the electrochemical reduction of CO<sub>2</sub> to valuable chemicals is of great interest. In the present study, cobalt-oxide nanodendrites were directly grown on a Co substrate and systemically studied towards the electrochemical reduction of CO<sub>2</sub>. Our electrochemical measurements revealed that the formed Co nanodendrites exhibited superb catalytic activity in comparison to the Co-based catalysts reported in the literature, with a small onset potential (−0.2 V vs RHE) and an extremely high current density for the CO<sub>2</sub> reduction. *In situ* electrochemical attenuated total reflection Fourier transform infrared spectroscopy was employed to elucidate the reduction reaction mechanism, revealing that the formation of formate at the Co nanodendrites proceeded through the formation of a carbon-bound adsorbed \*COO<sup>−</sup> intermediate. The innovative approach and the in-situ FTIR analysis reported in the present study would provide insights in the design and tuning of advanced electrocatalysts for energy and environmental applications.

## 1. Introduction

The continuous rise in carbon dioxide (CO<sub>2</sub>) concentration in the atmosphere is known to be a major cause of climate change. The use of CO<sub>2</sub> as a precursor in the production of synthetic fuels and other industrial chemicals offers a way to gradually decrease atmospheric CO<sub>2</sub> concentration and eventually closing the anthropogenic carbon cycle [1]. The conversion of CO<sub>2</sub> to valuable industrial chemicals, such as carbon monoxide (CO), formic acid (HCOOH) and methane (CH<sub>4</sub>), using electrochemical techniques has attracted attention due to two main advantages: (i) the technique can be coupled with renewable energy to drive the electrolytic process; and (ii) the electrode potential, electrolyte type, pH, temperature, and catalyst can be controlled to direct the reduction process towards a desired product [2,3]. Metal-based catalysts have been shown to be especially effective in electrochemical reduction of CO<sub>2</sub> to low-carbon chemicals. Due to their unique surface morphologies, nanostructured metal surfaces are essential for increasing the number of active sites and optimizing catalytic performance [3–6]. Metallic catalysts such as Au, Ag, Cu, Pd and Pt have shown high CO<sub>2</sub> conversion efficiencies [7–14]. However, copper, for instant, has been shown to suffer from low product selectivity [11,15,16]. Pt, Ni and Fe have been found susceptible to activity loss due to blockage of active

sites, and thus more efficient for hydrogen evolution reaction (HER) [17–19]. Whereas, noble-metal catalysts are expensive and in limited supply for a large-scale production [20,21]. The design of electrocatalysts that have high product selectivity, long-term stability and low costs is critical to the realization of a CO<sub>2</sub> reduction electrochemical cell designated for industrial use.

The search for a cost-effective metal has led to the exploration of cobalt-based materials as a viable catalyst for CO<sub>2</sub> reduction reaction (CO<sub>2</sub>RR). Although cobalt (Co) is widely used as a catalyst for electrochemical water-splitting [17,22,23], recent findings show that Co and Co-oxides can lead to the reduction of CO<sub>2</sub> to formate with high faradaic efficiencies [24–29]. Gao et al. reported partially oxidized atomic layers of Co to reduce CO<sub>2</sub> to formate with approximately 90% efficiency at −0.85 V vs. SCE with current density of 10 mA/cm<sup>2</sup> for over 40 h [24], while ultrathin layer (1.72 nm) of Co<sub>3</sub>O<sub>4</sub> was reported to produce formate at −0.88 V vs. SCE with 60% Faradaic efficiency for over 20 h [25]. Aljabour et al. reported Co<sub>3</sub>O<sub>4</sub> nanofibers with 65% conversion efficiency to CO and 27% to formate at −1.5 V vs. SCE. The nanofibers were reported to be stable for 8 h with 0.5 mA/cm<sup>2</sup> current density [26]. While the mentioned reports used pristine Co/Co-oxide as the catalyst, Sekar et al. fabricated Co<sub>3</sub>O<sub>4</sub> nanocubes supported on nitrogen-doped graphene with 83% formate Faradaic efficiency at −0.82 V vs. SCE

\* Corresponding author.

E-mail address: [aicheng@uoguelph.ca](mailto:aicheng@uoguelph.ca) (A. Chen).

<sup>1</sup> ORCID: 0000-0002-2239-6785

<https://doi.org/10.1016/j.apcatb.2021.120761>

Received 8 August 2021; Received in revised form 20 September 2021; Accepted 25 September 2021

Available online 28 September 2021

0926-3373/© 2021 Elsevier B.V. All rights reserved.

with 10.50 mA/cm<sup>2</sup> current density [27]. These findings imply that the atomic and nano scale structures not only increase the exposed number of active sites and allow faster mass transport from the electrolyte to the surface of the catalyst, but also provide an optimal electronic state in which CO<sub>2</sub> can bind and be reduced to formate [28]. However, there are two major issues with these reports. First, the catalysts were supported on a substrate such as a glassy carbon electrode or fluorine-doped tin oxide (FTO) conductive glass and thus required the aid of polymer binders and additives that might block active sites [30–32]. Second, none of these reports provide a detailed mechanistic insight into how CO<sub>2</sub> is being reduced to formate. The lack of fundamental understanding of the catalytic reduction mechanisms leads to the inability to further tune the chemical and physical properties of the catalyst and to improve its activity and selectivity [33].

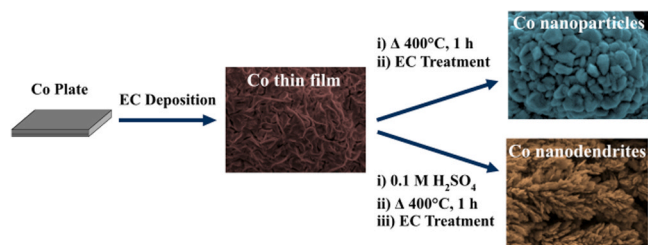
In this study, self-supported nanostructured Co-oxide catalysts were fabricated without the use of any polymer bindings and additives. A cobalt nanodendrites (CoNDs) were optimized to attain a large electrochemically active surface area, high stability, and catalytic activity for the electrochemical reduction of CO<sub>2</sub> to formate. This study examined how the composition and morphology of the Co-oxide nanostructured surfaces affected their catalytic activity in the CO<sub>2</sub>RR and provided fundamental understanding of the catalytic reduction mechanisms using in-situ electrochemical attenuated total reflection Fourier transform infrared (ATR – FTIR) spectroscopy. This technique was used to provide molecular-level structural information about the intermediates and products with enhanced sensitivity during the electrochemical CO<sub>2</sub>RR.

## 2. Experimental section

The details on chemicals and materials, surface characterization, and electrochemically active surface area (EASA) determination are described in the [Supporting Information](#).

### 2.1. Fabrication of Co-based nanomaterials

**Scheme 1** illustrates the fabrication procedures of the Co thin film (CoTF), Co nanoparticles (CoNPs) and CoNDs. Cobalt substrates (1.0 cm<sup>2</sup>) were chemically etched in 35% HNO<sub>3</sub> for 1 min and thoroughly rinsed with pure H<sub>2</sub>O. The substrates were cleaned with acetone using an ultrasonic bath for 10 min followed by sonication in pure H<sub>2</sub>O for additional 10 min. A 0.25 cm<sup>2</sup> Co plate was used as the anode in the electrochemical (EC) deposition and was also cleaned using the above procedure along with the cobalt substrates. The CoTF was fabricated by EC deposition in a three-electrode cell containing a 0.1 M CoSO<sub>4</sub>·7H<sub>2</sub>O solution using Ag/AgCl (3 M KCl) as the reference electrode. Chronoamperometry was conducted at –1.2 V vs. Ag/AgCl for 20 min. The CoNPs were produced by annealing the CoTF at 400 °C for 1 h, followed by electrochemical reduction (EC treatment) at –1.4 V vs. Ag/AgCl for 10 min in a CO<sub>2</sub>-saturated 0.1 M KOH solution (8.0 pH). To form the CoNDs, 20 μL of 0.1 M H<sub>2</sub>SO<sub>4</sub> was dropped on the CoTF surface in increments of 10 μL and air-dried. The acid treated surface was then annealed at 400 °C for 1 h and followed by the EC treatment.



**Scheme 1.** Schematics of the fabrication pathways of the Co thin film (CoTF), Co nanoparticles (CoNPs), and Co nanodendrites (CoNDs).

### 2.2. Electrochemical characterization

HEKA PG 610 Potentiostat was used for the electrochemical experiments (e.g., linear sweep voltammetry (LSV) and chronoamperometry (CA)) in a two-compartment cell system. A platinum coil was used as the counter electrode and was cleaned by flame annealing and thoroughly washed with deionized H<sub>2</sub>O. The Pt counter electrode was separated from the working and reference electrodes in a H-cell configuration using an ionic exchange membrane (AMI-7001 Membranes International Inc.). Ag/AgCl (3.0 M KCl) was used as the reference electrode and the measured potential was converted to the reversible hydrogen electrode (RHE) scale (E vs. RHE) using the following equation:

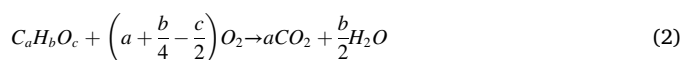
$$E(\text{vs. RHE}) = E(\text{vs. Ag/AgCl}) + 0.0591V \times \text{pH} + 0.210V \quad (1)$$

A CO<sub>2</sub>-saturated 1 M KOH solution was used as the electrolyte for all the CO<sub>2</sub>RR experiments. The pH of the electrolyte dropped to 8.0 after 15 min of purging with CO<sub>2</sub> gas. For comparison, the working electrodes coated with the fabricated catalysts were also tested for the hydrogen evolution reaction (HER), where the measurements were conducted in a similar setup as the CO<sub>2</sub> reduction experiments, but the electrolyte solution was changed to Ar-saturated 0.1 M K<sub>2</sub>SO<sub>4</sub> with adjusted pH of 8.0.

### 2.3. Product analysis

Gas and liquid products of the electrochemical reduction of CO<sub>2</sub> were collected in a two-compartment cell with an anionic exchange membrane (AMI-7001 Membranes International Inc.) to separate the cathode and anode cell compartments. The working electrode and reference electrode (Ag/AgCl) were positioned in the cathode compartment along with CO<sub>2</sub> gas inlet to continuously purge the 1 M KOH solution during the electrolysis. Pt counter electrode was placed in the anode cell compartment. Gas chromatography (GC) was employed for analyzing the gas products generated from the CO<sub>2</sub>RR. The Shimadzu GC-2014 was equipped with ShinCarbon ST column, a flame ionization detector (FID), and thermal conductivity detector (TCD). To identify and quantify the liquid products, a 600 MHz Bruker Avance III NMR Spectrometer with a Cryoprobe was employed to record the <sup>1</sup>H NMR spectra. A mixture of the electrolyte solution sample and 20% D<sub>2</sub>O was used, where 0.05 μL TMS (tetramethylsilane) was added to the sample as the internal reference. The amount of formate produced (mmol/h) was measured in the obtained liquid products after 60 min of the CO<sub>2</sub>RR in a CO<sub>2</sub>-saturated 1 M KOH solution at the CoTF, CoNP, and CoND electrodes. Calibration curve was established using a series of standard solutions containing known concentration of formate ions between 0 to 1.0 mmol.

A chemical oxygen demand (COD) analysis [12] was conducted on the liquid products collected after an hour of chronoamperometry at –0.3 V, –0.4 V, –0.5 V and –0.6 V vs. RHE in a CO<sub>2</sub>-saturated 1 M KOH solution for each electrode. The COD was conducted using 174–334 accu-TEST<sup>TM</sup> standard range (5–150 mg/l) containing chromic acid solution for quantitative determination of reduction products. 1.0 mL solution of liquid products was inserted into each COD vial, heated to 150 °C for 2 h and then allowed to cool to room temperature. To establish the COD values, the results were subtracted from the values of a blank solution (CO<sub>2</sub>-saturated 1 M KOH solution 8.0 pH). The UV absorbance was recorded at 420 nm using an HACH-DR 2800 portable spectrophotometer. The Faradaic Efficiency (FE%) was calculated from the COD analysis by determining the total number of electrons that are consumed in the electrochemical reduction of CO<sub>2</sub>. In this method the CO<sub>2</sub> reduction products are chemically oxidized to completion via the following chemical equation [12]:



where *a*, *b*, and *c* represent the stoichiometric ratio of carbon, hydrogen, and oxygen, respectively. Since four electrons are being transferred per

O<sub>2</sub> molecule:



the following equation can be used to calculate the charge ( $Q_{\text{COD}}$ ) used for the formation of the liquid products:

$$Q_{\text{COD}} = \text{COD} \times \frac{4FV}{32000} \quad (4)$$

where COD is the actual value obtained from the UV spectrophotometer corresponds to mg/L of O<sub>2</sub> consumed, F is the Faraday constant and V (L) is the volume of the electrolyte solution. The Faradaic efficiency is then calculated using the calculated COD charge ( $Q_{\text{COD}}$ ) and the overall charge ( $Q$ ) passed in the cell during CO<sub>2</sub> reduction:

$$\text{FE}_{\text{COD}}\% = \frac{Q_{\text{COD}}}{Q} \times 100 \quad (5)$$

#### 2.4. In situ electrochemical FTIR study

The in situ attenuated total reflection Fourier transform infrared (ATR–FTIR) spectroscopic study was conducted in an external reflection configuration as shown in the supporting information (Scheme S1). In this configuration the working electrode coated with the fabricated catalyst was placed against the light-guiding crystal with a high refractive index (ZnSe hemisphere window) and effectively trapping a thin layer of electrolyte (1–10 μm thickness) between itself and the crystal [11,13,34,35]. This approach allows the detection of both adsorbed species and electrolyte species trapped in the thin layer. These experiments were carried out using an 8700 Nicolet Fourier transform infrared spectrometer with liquid N<sub>2</sub>-cooled HgCdTe (MCT) detector. A Ti rod was used as a holder for the fabricated CoNDs, which were attached to the bottom of the rod with the catalyst facing the crystal window. A graphite rod was used as the counter electrode and Ag/AgCl (3.0 M KCl) was used as the reference electrode. To avoid interference from existing bicarbonate/carbonate species, 0.1 M K<sub>2</sub>SO<sub>4</sub> solution was used as the electrolyte made with either H<sub>2</sub>O or D<sub>2</sub>O. For the CO<sub>2</sub>RR experiments the electrolyte was purged with CO<sub>2</sub> gas for 20 min prior to the start of the measurement and was continually purged during the experiment. To monitor changes in signal intensity due to consumed or produced species, as well as to minimize spectral background, a subtractively normalized interfacial FTIR spectroscopic (SNIFTIRS) method was employed. In this method, spectra were acquired at base potential ( $E_1$ ) and sample potential ( $E_2$ ) and their difference was divided by the base spectrum at  $E_1$  as follows:

$$\frac{\Delta R}{R} = \frac{R(E_2) - R(E_1)}{R(E_1)} \quad (6)$$

where  $R(E_1)$  and  $R(E_2)$  are the reflection single-beam spectra at the applied potential  $E_1$  and  $E_2$ , respectively. The resulting spectrum is reported as a relative change in electrode reflectivity ( $\frac{\Delta R}{R}$ ) as a function of wavenumber (cm<sup>-1</sup>). In this study, spectra were obtained with 4 cm<sup>-1</sup> resolution and averaged over 32 scans for the potential-dependant experiments and averaged over 8 scans for the time-dependent experiments. The base spectrum ( $R(E_1)$ ) was obtained at 0.0 V vs. RHE while the sample spectrum ( $R(E_2)$ ) was collected at each 0.1 V potential step between -0.1 to -0.8 V vs. RHE. According to Eq. (6), a negative-oriented peak appears if  $R(E_2)$  is greater than  $R(E_1)$ . That is the case when a new species is being produced and detected in the sample spectrum at the applied potential  $E_2$ . However, a positive-oriented peak is observed when  $R(E_1)$  is greater than  $R(E_2)$ . That happens when the detected species is consumed at the sample potential  $E_2$ .

### 3. Results and discussion

#### 3.1. Surface and electrochemical characterization of the Co-based electrodes

The surface morphology of the formed CoTF, CoNPs and CoNDs was imaged using SEM and their composition was characterized using EDX. Fig. 1 shows the SEM images of the formed Co-based catalysts recorded at 500 and 30 K magnification. The low-magnification SEM images (Fig. 1A, C and E) revealed that the thin film and the particles were uniformly distributed on the Co substrates. The CoTF was initially deposited on a Co substrate via electrochemical deposition; some cracks were observed at the high-magnification SEM image (Fig. 1B). The formed CoTF was then calcinated at 400 °C in air for 1 h and electrochemically (EC) reduced to form CoNPs. As shown in Fig. 1C, the surface structure was dramatically changed; particles with a wide range of dimensions were formed on the surface. Upon a close inspection (Fig. 1D), each particle was comprised of a large number of nanoparticles. When the CoTF was treated with 0.1 M H<sub>2</sub>SO<sub>4</sub> prior to the calcination step, CoNDs uniformly formed on the surface (Fig. 1 E & F), showing that H<sub>2</sub>SO<sub>4</sub> acted as an etching agent on the CoTF surface and created the dendritic structure.

Fig. 2A depicts the EDX spectra of the Co substrate, CoTF, CoNPs and CoNDs; Table S1 summarizes the calculated atomic percent of Co and O of each electrode. The CoTF was shown to have slightly more oxide formation than the Co substrate, with an increase in oxygen content from 1.4 to 8.9 at. percent. A significant increase in oxide formation was observed in the CoNPs and CoNDs with 16.8 and 34.9 oxygen atomic percent, respectively. Despite the subsequent EC reduction treatment, it is expected that the oxide remaining on the surface resulted from exposure to air. The XRD patterns displayed in Fig. 2B compare the crystalline phases of the synthesized CoTF, CoNPs and CoNDs to the pristine Co substrate. The crystalline phases: (1 0 0), (0 0 2), (1 0 1) and (1 1 0) of the pristine Co substrate [36] appeared in the CoTF, CoNP and CoND electrodes. In addition to the Co crystalline phases, (1 1 1), (2 0 0) and (2 2 0) were also observed in the CoNP and CoND patterns and were found to correspond to CoO [36,37]. These results showed that prior to the annealing step, the CoTF was mainly comprised of elemental cobalt (Co<sup>0</sup>). However, after being annealed at 400 °C in the air, the formed CoNPs and CoNDs were comprised of a mixture of Co<sup>0</sup> and Co(II).

Fig. S1A displays the XPS survey scans of the cobalt plate, CoTF, CoNP and CoND electrodes; the atomic percentages of Co and oxygen were calculated and listed in Table S2. It is evident that the surfaces were highly oxidized; even the pristine cobalt plate showed a high oxygen content (72.7%) compared to only 27.3% cobalt. However, there was no notable difference of the oxygen atomic percentage among the four samples as Co is active and it can be easily oxidized in the air. The high-resolution Co 2p<sub>3/2</sub> spectrum of the CoNDs is shown in Fig. S1B. Using the peak fitting parameters outlined by Biesinger et al. [38], it was found that a convolution of Co<sub>3</sub>O<sub>4</sub> and Co(OH)<sub>2</sub> peaks best fitted the Co 2p<sub>3/2</sub> peaks of all the CoTF, CoNP, and CoND electrodes. The percent composition of Co<sub>3</sub>O<sub>4</sub> and Co(OH)<sub>2</sub> in CoTF, CoNPs and CoNDs electrodes are summarized in Table S3. It was determined by the XRD that CoNPs and CoND are most likely a mixture of Co<sup>0</sup> and CoO. However, the peak-fitting analysis revealed that the surface of the electrodes contained 60–80% Co(OH)<sub>2</sub> (Co<sup>2+</sup>) and 20–40% Co<sub>3</sub>O<sub>4</sub> (Co<sup>2+</sup> and Co<sup>3+</sup>), which was consistent with the results reported in the literature [38–40]. He et al. conducted in situ X-ray absorption near-edge spectroscopy (XANES) of Co<sub>3</sub>O<sub>4</sub> nanoparticles during the CO<sub>2</sub>RR in CO<sub>2</sub>-saturated 0.5 M KHCO<sub>3</sub> solution. They noted that at potentials between -0.1 to -0.4 V vs. RHE the absorption edge of the Co peak of Co<sub>3</sub>O<sub>4</sub> started to resemble the pristine Co peak [39]. Han et al. also observed a shift in the *operando* ambient-pressure XPS results of a Co(OH)<sub>2</sub> thin-film electrode towards Co<sup>0</sup> when -0.34 V vs. RHE was applied in 0.1 M KOH solution [40].

The electrochemically active surface areas (EASAs) of the CoTF,

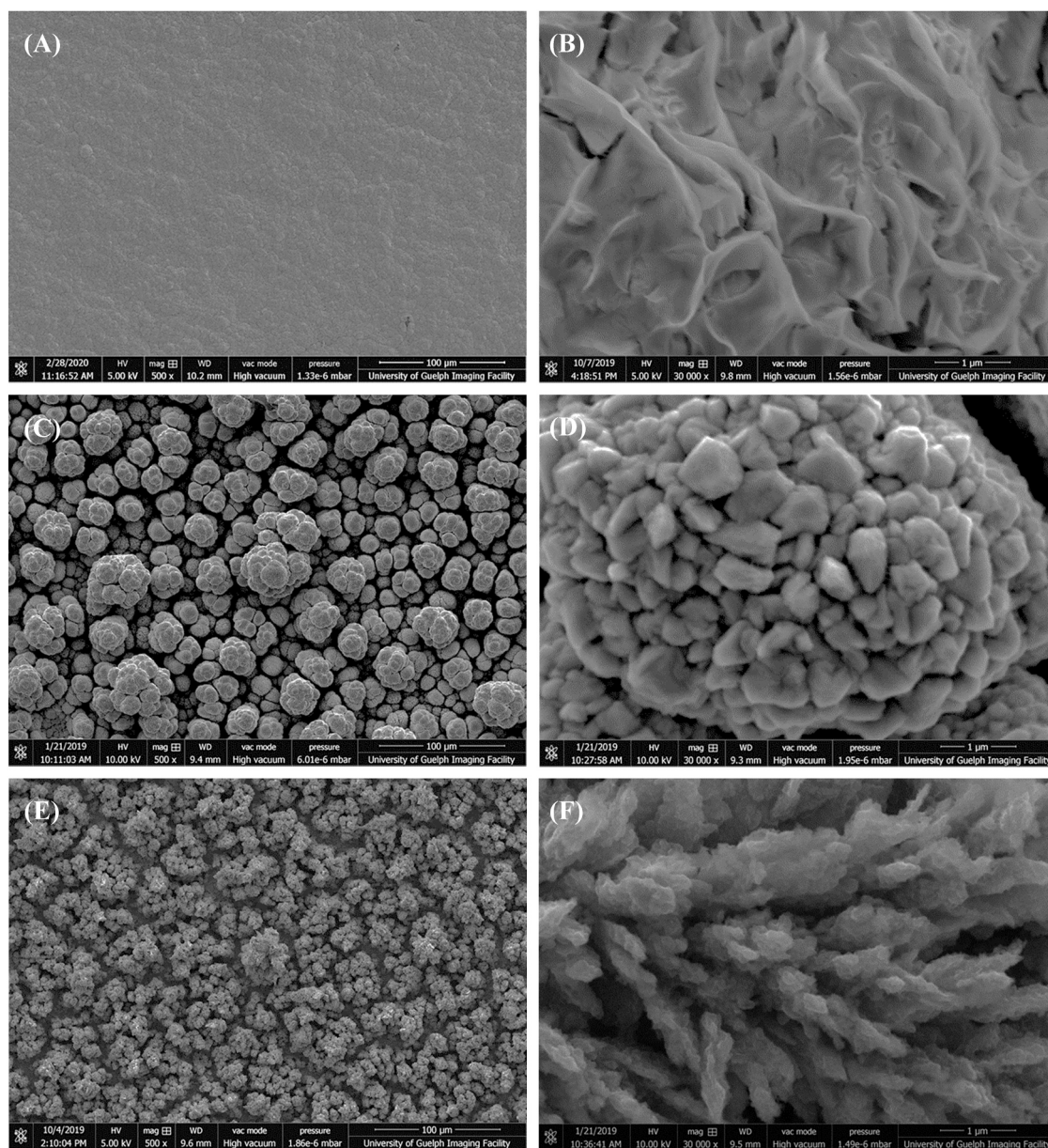


**Fig. 1.** Scanning electron microscopic (SEM) images of the CoTF (A and B), CoNPs (C and D) and CoNDs (E and F) at 500x (A, C and E) and 30,000x (B, D and F) magnification.

CoNP, and CoND electrodes were determined with respect to the smooth pristine Co substrate by measuring the double-layer capacitance in a  $\text{CO}_2$ -saturated 1 M KOH electrolyte (pH 8.0). The CVs were recorded in a potential range where no Faradaic reaction occurred, and the corresponding charging/discharging current density ( $\Delta j$ ) was plotted against the applied scan rate (Fig. S2). Both CoND and CoNP electrodes exhibited higher  $\Delta j$  values at the different scan rates compared to the CoTF and Co electrodes, indicating that CoNDs and CoNPs possessed larger double-layer capacitances. The current density was plotted against the scan rates for each electrode, resulting in a linear relation with high correlation coefficients ( $R^2$ ) varying from 0.998 to 0.999. The capacitance was determined from the slope of each linear regression (Fig. S2B); the CoNDs achieved the highest double-layer capacitance compared to the other Co electrodes. The double-layer capacitance and the surface roughness factor of the different Co-based electrodes are listed in Table S4, showing that the EASA was increased in the following order:  $\text{Co} < \text{CoTF} < \text{CoNP} < \text{CoND}$ , where the EASA of the CoND was 7.49 times greater than that of the pristine Co plate.

### 3.2. Electrochemical $\text{CO}_2$ reduction and product analysis

The electrocatalytic activity of the fabricated Co electrodes in the  $\text{CO}_2$ RR was studied using linear sweep voltametric (LSV) and chronoamperometric (CA) techniques in a  $\text{CO}_2$ -saturated 1 M KOH (pH 8.00) solution. The solid lines in Fig. 3A represents the LSV curves of the CoTF (red), CoNPs (blue), and CoNDs (green) compared to that of a pristine Co substrate (black) at a 20 mV/s scan rate. Both CoNDs and CoNPs showed early potential onset compared to the CoTF and Co substrate, while CoNDs demonstrated the highest current density compared to the other Co electrodes. The steady-state current densities of these electrodes are shown in the CA plots (Fig. 3B) measured at  $-0.7$  V vs. RHE. The CoNDs achieved the highest cathodic current density at  $-272 \text{ mA/cm}^2$  compared to the CoNPs ( $-195 \text{ mA/cm}^2$ ), CoTF ( $-83 \text{ mA/cm}^2$ ) and Co substrate ( $-11 \text{ mA/cm}^2$ ). The superior electrocatalytic activity of the CoNDs in comparison to the other Co electrodes indicates that the fabricated Co nanodendrites is a promising electrocatalyst for the  $\text{CO}_2$  reduction.

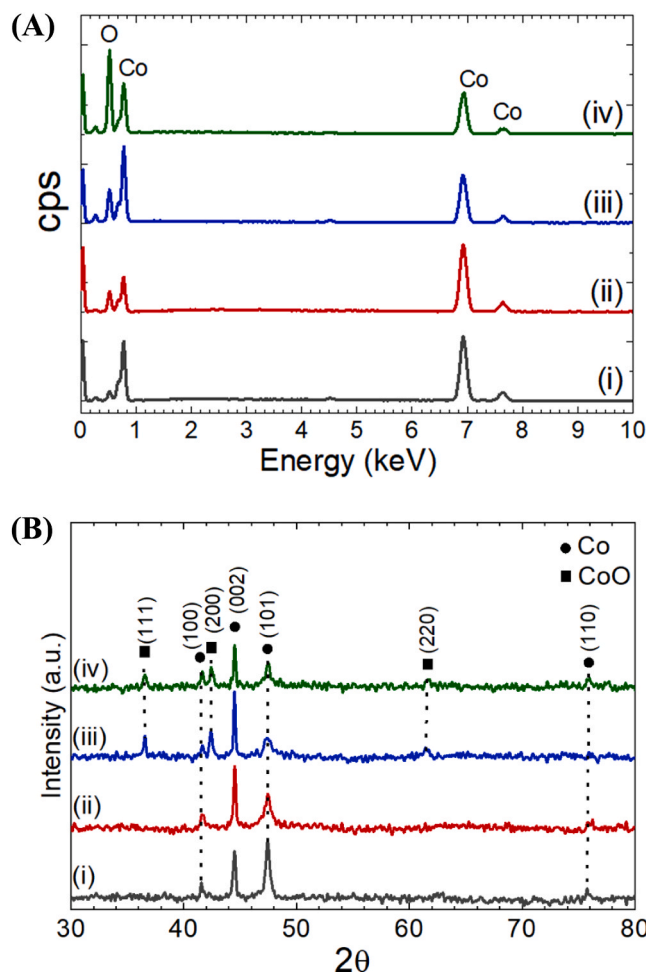


**Fig. 2.** (A) EDX and (B) XRD patterns of (i) Co substrate, (ii) CoTF, (iii) CoNPs, and (iv) CoNDs.

The LSVs of the fabricated Co electrodes were also recorded in an Ar-saturated 0.1 M  $\text{K}_2\text{SO}_4$  solution (pH was adjusted to be 8.00 by adding a small volume of 0.01 M KOH) to evaluate their catalytic activity towards the competing hydrogen evolution reaction (HER). The dash lines in Fig. 3A and B represent the LSV and CA obtained in the Ar-saturated 0.1 M  $\text{K}_2\text{SO}_4$  solution, respectively. As shown in Fig. 3A, the potential onset for the HER was at a more negative potential (approximately  $-0.5$  V) compared to the  $\text{CO}_2\text{RR}$ . However, the difference in the potential onset of HER and  $\text{CO}_2\text{RR}$  is most significant in the case of the CoNPs and CoNDs. It is interesting to note that although the order of the steady-state current densities (shown in Fig. 3B) of the Co electrodes for HER and  $\text{CO}_2\text{RR}$  was similar, much higher current was generated for the  $\text{CO}_2\text{RR}$ . The CoNDs achieved the highest current density at  $-71 \text{ mA/cm}^2$  compared to the CoNPs ( $-53 \text{ mA/cm}^2$ ), CoTF ( $-21 \text{ mA/cm}^2$ ) and Co substrate ( $-7 \text{ mA/cm}^2$ ), indicating a consistent trend in enhancing the catalytic activity by increasing the surface-to-volume ratios and thus exposing more active sites.

Fig. 4A shows the CA plots obtained during the one-hour  $\text{CO}_2\text{RR}$  at applied potentials of 0.0,  $-0.3$ ,  $-0.4$ ,  $-0.5$  and  $-0.6$  V vs. RHE over the CoNDs. The gas products generated from the  $\text{CO}_2\text{RR}$  were analyzed using GC, revealing that no notable amount of CO or  $\text{CH}_4$  gas was formed. However, the  $^1\text{H}$  NMR spectra (Fig. 4B) revealed a peak at 8.43 ppm which corresponds to formate proton [41,42]. The integrated area of the formate peaks in the  $^1\text{H}$  NMR spectra was plotted against the applied potential (Fig. 4C), revealing that the integrated peak increased from  $-0.3$  to  $-0.5$  V and decreased at  $-0.6$  V. Quantitative analysis of the liquid products at  $-0.4$  and  $-0.5$  V vs. RHE showed the highest

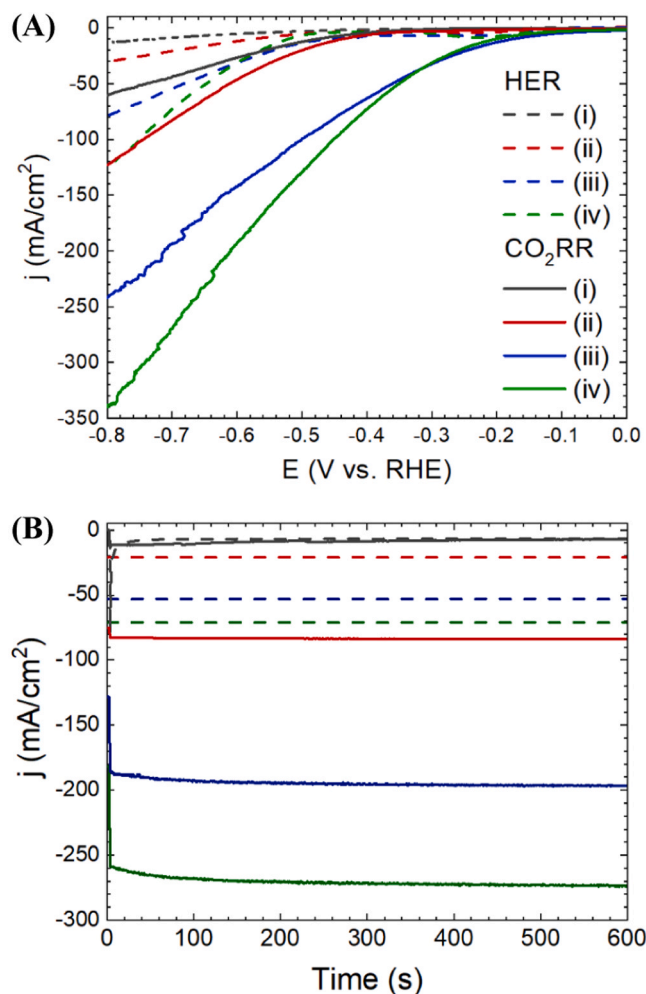


**Fig. 3.** (A) LSV of (i) Co substrate, (ii) CoTF, (iii) CoNP, and (iv) CoND electrodes recorded at  $20 \text{ mV/s}$  scan rate. The dashed lines represent HER experiments conducted in Ar-saturated 0.1 M  $\text{K}_2\text{SO}_4$  and solid lines represent  $\text{CO}_2\text{RR}$  experiments conducted in  $\text{CO}_2$ -saturated 1 M KOH; (B) corresponding CA of the electrodes measured at  $-0.7$  V vs. RHE for 600 s.

formate yield of 0.43 and 0.59 mmol/h, respectively, for CoNDs (Fig. 4D). This trend was consistent with the chemical oxygen demand (COD) analysis of the liquid products using the CoTF, CoNP and CoND catalysts after one-hour electrolysis. As shown in Fig. S4, the calculated  $\text{FE}_{\text{COD}}\%$  was the highest for the CoNDs at  $-0.4$  V (49.5%) and second highest at  $-0.5$  V (32.4%). Table S5 compares the performance of reported Co and Co-oxide catalysts for the electrochemical reduction of  $\text{CO}_2$  to produce formate recently reported in the literature. As can be seen, the CoNDs developed in the present study exhibited much higher current density at a much lower overpotential with a reasonably good Faradaic efficiency.

### 3.3. Potential-dependent in situ electrochemical FTIR study

In situ electrochemical ATR-FTIR spectra were recorded to analyze the intermediates and products formed during the electrochemical reduction of  $\text{CO}_2$ . The  $\text{CO}_2\text{RR}$  and HER are the two primary reactions that can occur in the potential range of 0.0 to  $-1$  V vs. RHE [29]. To identify and monitor the consumed and produced species under the reaction condition, SNIFTIR spectra were recorded at different applied potentials (0.0 to  $-0.80$  V vs. RHE) in Ar-saturated 0.1 M  $\text{K}_2\text{SO}_4$  for the HER and  $\text{CO}_2$ -saturated 0.1 M  $\text{K}_2\text{SO}_4$  electrolyte solution for the  $\text{CO}_2\text{RR}$ . The spectrum collected at 0.0 V vs. RHE for each potential-dependent experiment was set as the reference where no electrochemical reaction

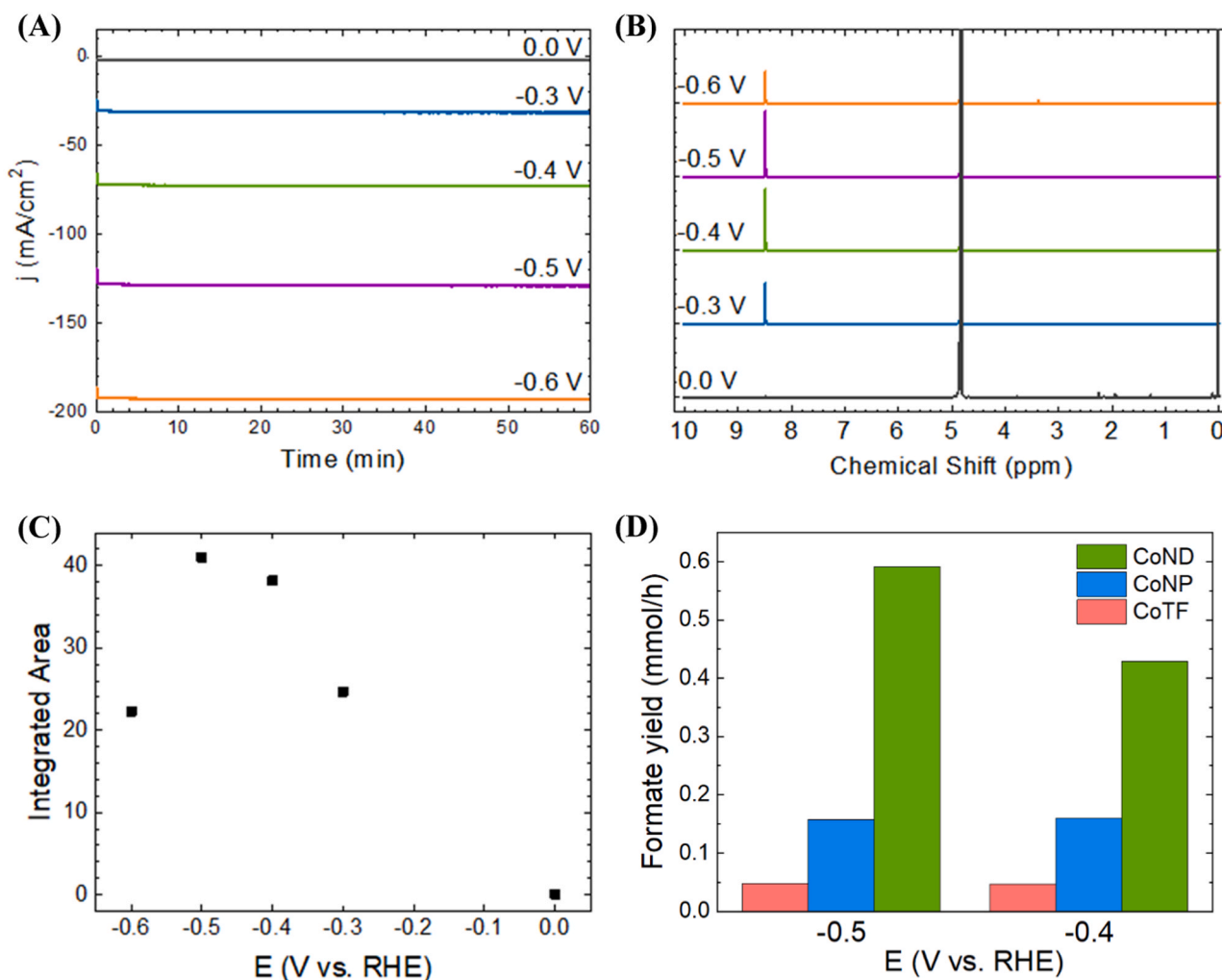


**Fig. 4.** (A) CA of the CoNDs measured at  $-0.3$  to  $-0.6$  V vs. RHE for 60 min in a CO<sub>2</sub>-saturated 1 M KOH; (B) <sup>1</sup>H NMR spectra of the liquid products from the CO<sub>2</sub>RR at 0.0,  $-0.3$ ,  $-0.4$ ,  $-0.5$ ,  $-0.6$  V vs. RHE for 60 min at the CoNDs, where tetramethylsilane (TMS) was used as the reference; (C) integrated peak area of the formate peak at 8.45 ppm from Fig. 4B; and (D) Formate yield (mmol/h) determined by <sup>1</sup>H NMR analysis of the liquid products after 60 min of the CO<sub>2</sub>RR in a CO<sub>2</sub>-saturated 1 M KOH solution at  $-0.4$  and  $-0.5$  V vs. RHE for the CoTF, CoNP, and CoND electrodes.

was expected to occur. Fig. S5A shows the CO<sub>2</sub>RR reference spectra of CO<sub>2</sub>-saturated 0.1 M K<sub>2</sub>SO<sub>4</sub> made with H<sub>2</sub>O and D<sub>2</sub>O. In the SNIFTIR spectrum, a negatively oriented peak was observed when new species formed while a positively oriented peak was seen when the detected species in the reference spectrum was consumed in the reaction. Fig. S6A displays the potential-dependent SNIFTIR spectra during HER on the surface of the CoNDs in an Ar-saturated 0.1 M K<sub>2</sub>SO<sub>4</sub> solution in H<sub>2</sub>O. The observed peaks correspond to the stretching mode  $\nu_s$  of H<sub>2</sub>O (3800–2800 cm<sup>-1</sup>) and H-O-H bending mode  $\nu_b$  (1645 cm<sup>-1</sup>) [43]. The positively oriented peaks indicated that water was consumed from the thin layer of solution trapped between the CoND catalyst and the ZnSe crystal. Fig. S6B shows the integrated peak area of the water stretch and bending mode as a function of the applied cathodic potential. In the potential range of  $-0.1$  to  $-0.5$  V, the water peaks remained unchanged, but their integrated area started to rise at  $-0.6$  V and continued to increase at  $-0.7$  and  $-0.8$  V. This increase in the peak integration at  $-0.6$  V was attributed to the onset potential of the HER on the CoND surface. Fig. 5A shows the potential-dependent SNIFTIR spectra during the CO<sub>2</sub>RR using the CoND electrode in a CO<sub>2</sub>-saturated 0.1 M K<sub>2</sub>SO<sub>4</sub> solution made with H<sub>2</sub>O. The positively oriented peak at 2343 cm<sup>-1</sup> corresponded to OCO asymmetric stretch  $\nu_{as}$  of CO<sub>2</sub> in solution [44]. In Fig. 5B, the integrated peak area of CO<sub>2</sub> was compared to those of  $\nu_s$ (H<sub>2</sub>O) at each applied potential. There was a small increase in the CO<sub>2</sub>

integrated peak area as the cathodic potential was increased from  $-0.2$  to  $-0.3$  V which signaled the onset of CO<sub>2</sub> consumption from the thin layer solution. There was a 71% rise in the integrated peak area between  $-0.3$  and  $-0.4$  V, and a maximum at  $-0.5$  V. When the potential increased from  $-0.5$  to  $-0.8$  V, the integrated peak area gradually dropped by 33%. Since the  $\nu_{as}$ (CO<sub>2</sub>) was still directed in the positive direction in the  $-0.5$  to  $-0.8$  V potential range, it was concluded that CO<sub>2</sub> was still being consumed, but its consumption declined with each potential step. In comparison, there was a moderate increase in the integrated peak area of  $\nu_s$  (H<sub>2</sub>O) between  $-0.1$  to  $-0.6$  V by 32%, and a significant rise between  $-0.6$  and  $-0.8$  V by 68%. This observation was consistent with the electrochemical results which pointed at a maximum efficiency for CO<sub>2</sub> reduction at  $-0.4$  and  $-0.5$  V compared to HER and a late potential onset of the HER relative to the CO<sub>2</sub>RR. It is important to note that no peaks were observed in the wavenumber region 1900–2100 cm<sup>-1</sup>, where linear or bridged CO peaks are typically expected to show in case of CO adsorbed on the surface [44–48]. This observation indicated two important findings regarding reaction mechanism of the CO<sub>2</sub>RR on the surface of the CoNDs. First, CO intermediates were not involved in the reduction process; and second, it provided additional support to the GC results which showed no CO gas peak.

The potential-dependant spectra from Fig. 5A were overlaid and focused on the 1800–1000 cm<sup>-1</sup> region in Fig. 5C for comparison. Since

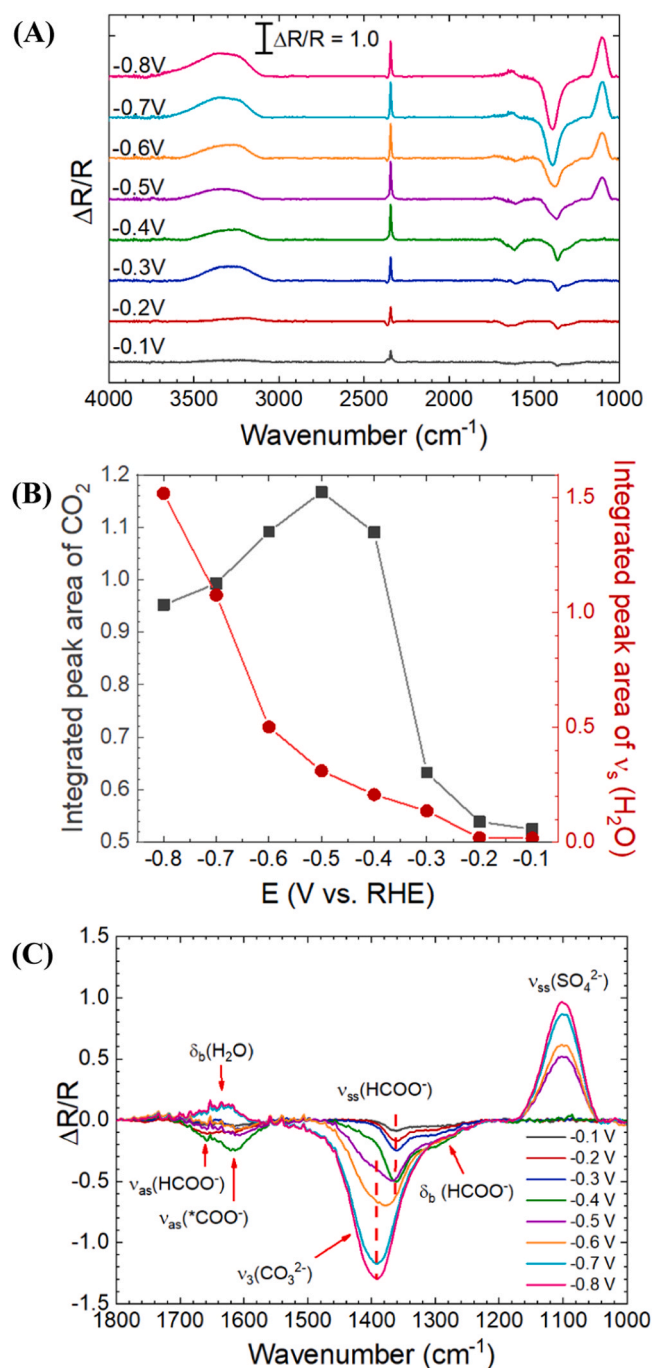


**Fig. 5.** (A) Potential-dependent SNIFTIRS spectra recorded during the CO<sub>2</sub> reduction at the CoND electrode in a CO<sub>2</sub>-saturated 0.1 M K<sub>2</sub>SO<sub>4</sub> solution in H<sub>2</sub>O in the potential range of -0.1 to -0.8 V vs. RHE; (B) integrated peak area of CO<sub>2</sub> (2300–2400 cm<sup>-1</sup>) in black, compared to that of the water stretch band (3000–3800 cm<sup>-1</sup>) in red, as a function of the applied potential; and (C) overlaid SNIFTIRS spectra in the range of 1800–1000 cm<sup>-1</sup>.

the CO<sub>2</sub>RR on the Co-based catalysts has never been reported using in situ electrochemical FTIR prior to this study, the shown peaks were assigned based on values found in literature with similar experimental conditions and using density functional theory (DFT) calculations [13, 44, 49–52]. The peaks at 1660, 1360, and 1285 cm<sup>-1</sup> were assigned to formate: C=O asymmetric stretch  $\nu_{as}(\text{HCOO}^-)$ , C–O symmetric stretch  $\nu_{ss}(\text{HCOO}^-)$ , and C–H bending mode  $\delta_b(\text{HCOO}^-)$ , respectively. The peak at 1614 cm<sup>-1</sup> was assigned to the asymmetric stretch  $\nu_{as}$  of the adsorbed intermediate  $^*\text{COO}^-$ . However, the peak at 1395 cm<sup>-1</sup> was more difficult

to assign since it could represent either the symmetric stretch  $\nu_{ss}$  of  $^*\text{COO}^-$  or the C–O asymmetric stretch  $\nu_3$  of  $\text{CO}_3^{2-}$  ion in solution, or it might be the convolution of the two peaks [53,54]. Trends in peak evolution with respect to the applied potential was used to address this issue. The peaks corresponding to formate and  $^*\text{COO}^-$  were negatively oriented, indicating the formation of  $^*\text{COO}^-$  intermediate on the surface of CoNDs and formate ions in the thin layer solution. The positive peak at 1645 cm<sup>-1</sup> observed in the spectra at -0.7 and -0.8 V, was assigned to the H<sub>2</sub>O bending mode and was positive due to water consumption during the HER. The positive peak at 1100 cm<sup>-1</sup> was assigned to the symmetric stretch of sulfate ions in solution  $\nu_{ss}(\text{SO}_4^{2-})$ .

In Fig. 5C, under the applied potential range of -0.1 to -0.5 V, the peaks that correspond to formate ion seemed to develop (become more negative); however, at the potential range of -0.6 to -0.8 V, these peak intensities seemed to decrease (become less negative). At the critical potential between -0.5 V and -0.6 V, the peak at 1360 cm<sup>-1</sup> broadened and shifted towards 1395 cm<sup>-1</sup>. This observation was attributed to the heightened production of formate ions at -0.4 and -0.5 V and the subsequent decline in production at -0.6 to -0.8 V. The peak at 1395 cm<sup>-1</sup> was first observed at -0.5 V and increased in intensity (became more negative) as the cathodic potential was increased. Due to this deviation from the trend of the  $\nu_{as}(^*\text{COO}^-)$  peak at -0.5 V, it was concluded that the peak at 1395 cm<sup>-1</sup> was more likely to correspond to  $\nu_3(\text{CO}_3^{2-})$  in the potential range of -0.5 to -0.8 V. Time-dependent SNIFTIR experiments were conducted to further diagnose the trends between the assigned peaks. Fig. S5B compares the reflectance spectra of 0.1 M KHCO<sub>3</sub> (black) to 0.1 M K<sub>2</sub>CO<sub>3</sub> (red) solutions freshly prepared in H<sub>2</sub>O. As can be seen, the spectrum of K<sub>2</sub>CO<sub>3</sub> showed a peak at 1395 cm<sup>-1</sup>, whereas the peaks corresponding to KHCO<sub>3</sub> were at a lower wavenumber and thus eliminated the possibility of the observed peak at 1395 cm<sup>-1</sup> in Fig. 5C to belong to a bicarbonate species in solution [55].

To avoid interference of  $\delta_b(\text{H}_2\text{O})$  with the peaks under investigation, the in situ FTIR experiment of the CO<sub>2</sub>RR was repeated in a CO<sub>2</sub>-saturated 0.1 M K<sub>2</sub>SO<sub>4</sub> electrolyte solution prepared with D<sub>2</sub>O instead of H<sub>2</sub>O. Fig. 6A shows the potential-dependant SNIFTIRS spectra in the 2500–1000 cm<sup>-1</sup> region. The bending mode of deuterated water  $\nu_b(\text{D}_2\text{O})$  was observed at 1200 cm<sup>-1</sup> along with  $\nu_{ss}(\text{SO}_4^{2-})$  at 1100 cm<sup>-1</sup>. Fig. 6B shows the overlaid spectra in the 1800–1000 cm<sup>-1</sup> region. The peaks at 1626, 1367, and 1078 cm<sup>-1</sup> were assigned to formate: C=O asymmetric stretch  $\nu_{as}(\text{DCOO}^-)$ , C–O symmetric stretch  $\nu_{ss}(\text{DCOO}^-)$ , and C–D bending mode  $\delta_b(\text{DCOO}^-)$ , respectively. The peak at 1564 cm<sup>-1</sup> was assigned to the asymmetric stretch  $\nu_{as}$  of the adsorbed intermediate  $^*\text{COO}^-$ . The peak at 1405 cm<sup>-1</sup> was assigned to the C–O stretch  $\nu_3$  of  $\text{CO}_3^{2-}$  ion in solution where it was shifted to higher wavenumbers by 10 cm<sup>-1</sup> in D<sub>2</sub>O in comparison to H<sub>2</sub>O. Almost similar peak shift was observed in Fig. S5B when the 0.1 M K<sub>2</sub>CO<sub>3</sub> solution was prepared using D<sub>2</sub>O.

To monitor the peak intensities corresponding to formate,  $^*\text{COO}^-$  and carbonate ions, the absolute values were calculated and plotted against the applied potential as displayed in Fig. 6C. When the cathodic potential increased from -0.1 to -0.5 V,  $\nu_{as}(\text{DCOO}^-)$  and  $\nu_{ss}(\text{DCOO}^-)$  continually increased from 0.02 to 0.50 and 0.55, respectively. In contrast,  $\nu_{as}(^*\text{COO}^-)$  only increased from 0.02 to 0.10 in the same potential range. When the cathodic potential further increased from -0.5 to -0.7 V, the intensity of both  $\nu_{as}(\text{DCOO}^-)$  and  $\nu_{as}(^*\text{COO}^-)$  dropped to approximately 0.0 and remained relatively unchanged at -0.8 V. It was difficult to decipher the behavior of  $\nu_{ss}(\text{DCOO}^-)$  in the potential range of -0.7 V to -0.8 V since the peak was no longer distinguishable from the peak assigned to  $\nu_3(\text{CO}_3^{2-})$ . In agreement with the in situ FTIR experiment conducted in H<sub>2</sub>O, these results indicated that formate ions were produced in the potential range of -0.1 to -0.5 V and declined in production at -0.6 to -0.8 V.  $\nu_{as}(^*\text{COO}^-)$  peak followed the same trend as the formate peaks but its  $\Delta R/R$  values were much lower in comparison. This could be the result of the limited number of  $^*\text{COO}^-$  intermediate molecules adsorbed to the surface in comparison to the large number of formate ions trapped in the thin layer solution. While  $\nu_3(\text{CO}_3^{2-})$  peak was insignificant in the spectra taken at -0.1 V to

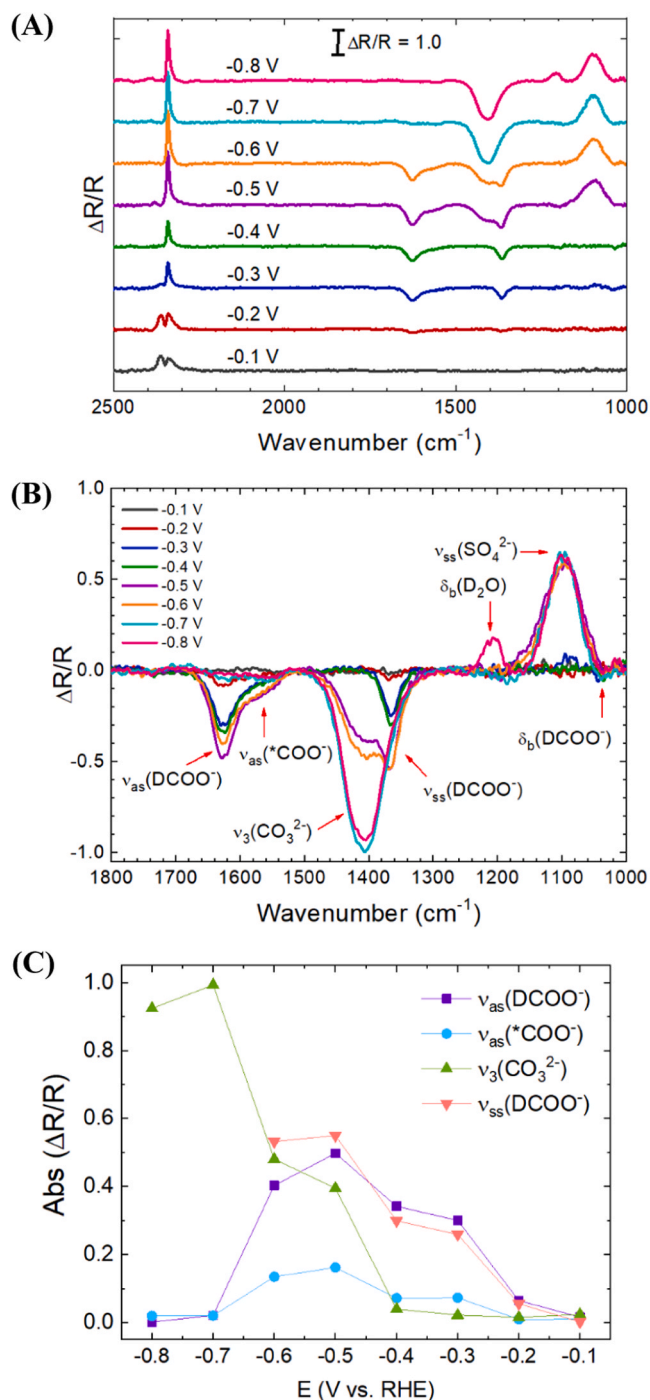


**Fig. 6.** (A) Potential-dependent SNIFTIRS spectra recorded during the  $\text{CO}_2$  reduction at the CoND electrode in a  $\text{CO}_2$ -saturated 0.1 M  $\text{K}_2\text{SO}_4$  solution in  $\text{D}_2\text{O}$  in the potential range of  $-0.1$  to  $-0.8$  V vs. RHE; (B) overlaid SNIFTIRS spectra in the range of  $1800 - 1000 \text{ cm}^{-1}$ ; (C) absolute values of the corresponding peak intensities calculated from Fig. 6B as a function of the applied potential.

$-0.4$  V, it increased by 99% between  $-0.4$  to  $-0.7$  V and only dropped slightly at  $-0.8$  V. The rapid increase of this peak indicated the  $\text{CO}_3^{2-}$  ion accumulation in the thin layer solution and thus a rise in the local pH as the equilibrium between carbonate and bicarbonate ions shifted towards carbonate ion.

### 3.4. Time-dependent in situ electrochemical FTIR study

To better understand the behavior of the adsorbed intermediate  $^*\text{COO}^-$ , formate and carbonate ions formed during  $\text{CO}_2\text{RR}$  on the CoND surface as a steady-state potential was applied, a time-dependent SNIFTIR experiment was obtained. The consumed and produced species were monitored through SNIFTIR spectra in a  $\text{CO}_2$ -saturated 0.1 M  $\text{K}_2\text{SO}_4$  electrolyte solution made with  $\text{D}_2\text{O}$ . The reference spectrum was collected at 0 s at 0.0 V vs. RHE. Then, a constant potential was applied for 100 s, and the spectrometer was set to collect spectra every 5 s. The time dependent SNIFTIR spectra recorded at  $-0.5$  and  $-0.7$  V are shown in Fig. 7A and B, respectively, and at  $-0.3$ ,  $-0.4$  and  $-0.6$  V are shown in Fig. S7. The calculated absolute values of the intensities ( $\Delta R/R$ ) of the peaks corresponding to formate and  $^*\text{COO}^-$  plotted as a function of time at  $-0.5$  and  $-0.7$  V are shown in Fig. 7C and D, respectively.

As  $-0.3$  V was applied (Fig. S7A), no major changes were observed in the spectra; however, at  $-0.4$  V (Fig. S7B), the formate and  $^*\text{COO}^-$  bands became more defined as the reaction progressed. The ratio between the  $\Delta R/R$  values of the peaks at  $1626$  and  $1367 \text{ cm}^{-1}$  were equivalent as the reaction progressed which further affirmed the peak assignments as  $\nu_{\text{as}}(\text{DCOO}^-)$  and  $\nu_{\text{ss}}(\text{DCOO}^-)$  bands, respectively. At  $-0.5$  V (Fig. 7C),  $\nu_{\text{as}}(\text{DCOO}^-)$  and  $\nu_{\text{ss}}(\text{DCOO}^-)$  bands gradually increased from 5 s to 45 s at a relatively similar rate. After 45 s, the intensity of both peaks reached a steady state at which minimal changes were observed: 3% increase for  $\nu_{\text{as}}(\text{DCOO}^-)$  and 14% increase for  $\nu_{\text{ss}}(\text{DCOO}^-)$  between 45 and 100 s. After the initial increase in intensity between 5 and 15 s,  $\nu_{\text{as}}(^*\text{COO}^-)$  and  $\nu_3(\text{CO}_3^{2-})$  did not rise and remained relatively unchanged between 15 and 40 s. After 45 s,  $\nu_3(\text{CO}_3^{2-})$  band increased in intensity by 106% and was as prominent as the peaks corresponded to formate ions in solution, whereas  $\nu_{\text{as}}(^*\text{COO}^-)$  only increased by 1%. These results showed that initially (before 45 s)  $^*\text{COO}^-$  intermediate and  $\text{CO}_3^{2-}$  were both produced at the same rate. However, a positively oriented peak was not observed at  $1350 \text{ cm}^{-1}$ , where a  $\text{DCO}_3^-$  peak was expected to appear. After 45 s,  $\text{CO}_3^{2-}$  ions started to accumulate and their concentration became equivalent to the concentration of the formate ions, while the  $^*\text{COO}^-$  intermediate concentration remained steady. Since the electrochemical study of the HER on the CoND surface showed no significant activity at  $-0.5$  V, it was unlikely that the increased concentration of the carbonate ion in the thin layer solution was due to the reaction of bicarbonate ions with the hydroxide ions produced from HER at  $-0.5$  V vs. RHE. Thus, it can be concluded that the production of carbonate ions was due to the deprotonation of bicarbonate ions in solution by the adsorbed intermediates and the production of formate ions. As  $-0.7$  V potential was applied to the CoND catalyst (Fig. 7D),  $\nu_{\text{as}}(^*\text{COO}^-)$  increased in intensity for the first 20 s, remained relatively unchanged from 20 to 25 s, and then dropped to its initial value.  $\nu_{\text{as}}(\text{DCOO}^-)$  and  $\nu_{\text{ss}}(\text{DCOO}^-)$  peaks reached a maximum within the first 20 s at relatively similar rates.  $\nu_{\text{as}}(\text{DCOO}^-)$  gradually dropped back to its initial value between 25 and 100 s, while  $\nu_{\text{ss}}(\text{DCOO}^-)$  only dropped by 37% from its initial value during this time period. This difference was due to the proximity of  $\nu_{\text{ss}}(\text{DCOO}^-)$  to  $\nu_3(\text{CO}_3^{2-})$  band which continued to develop as the reaction progressed. The drop in intensities of the  $^*\text{COO}^-$  intermediate and formate bands to zero indicated that formate ions were still produced in the thin layer solution, but their production slowed between 35 and 100 s. As was shown in the potential-dependant SNIFTIR spectra recorded during the HER (Fig. S6), the HER was prominent at  $-0.7$  V and it was concluded that the formate ions migrated from the thin layer solution to the bulk electrolyte due to the turbulence created by the hydrogen gas bubbles. As can be seen, the  $\nu_3(\text{CO}_3^{2-})$  band steadily increased as the reaction progressed. In contrast to the experiment conducted at  $-0.5$  V, it was believed that the rapid production of the carbonate ion at  $-0.7$  V was not only due to bicarbonate ions involvement in the  $\text{CO}_2\text{RR}$ , but also their reactions with hydroxide ions produced during the HER.

Fig. S8 compares the curves of the absolute values of the intensities of  $\nu_{\text{as}}(\text{DCOO}^-)$  and  $\nu_3(\text{CO}_3^{2-})$  bands as a function of time at each applied

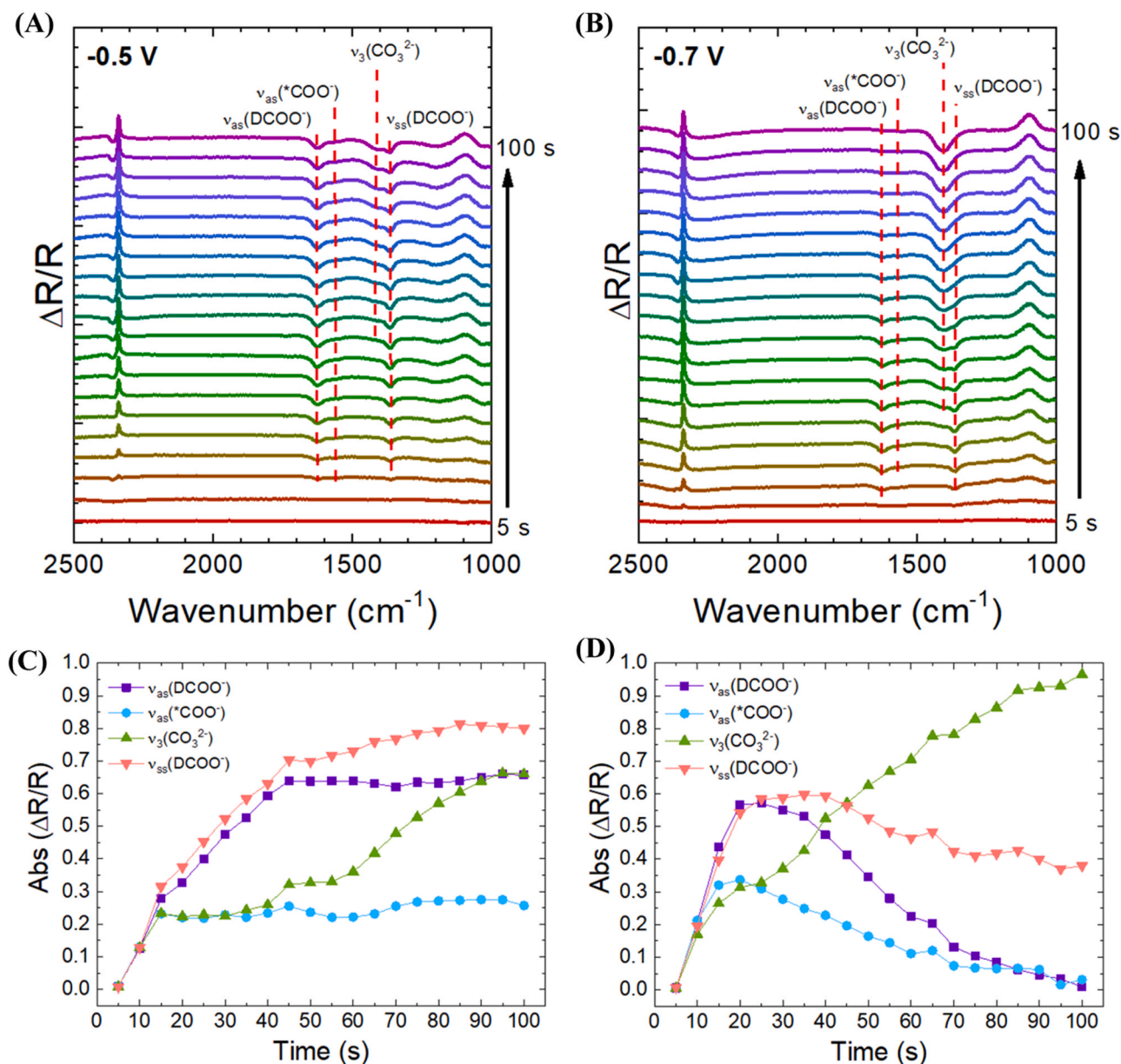


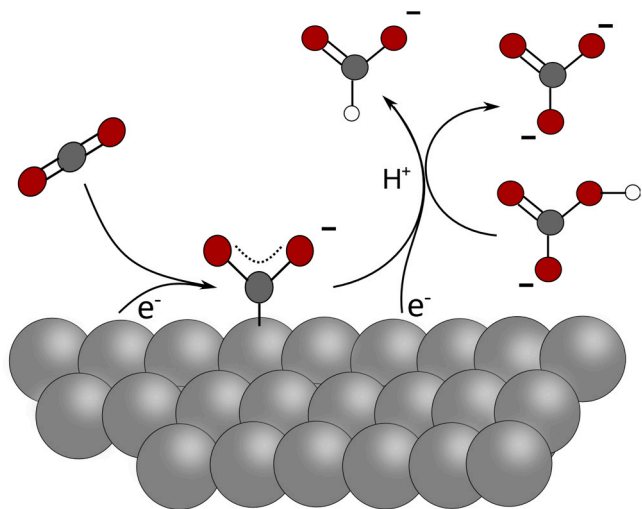
**Fig. 7.** Time-dependent SNIFTIR spectra recorded during the CO<sub>2</sub> reduction at the CoND electrode in a CO<sub>2</sub>-saturated 0.1 M K<sub>2</sub>SO<sub>4</sub> solution in D<sub>2</sub>O at (A) -0.5 V and (B) -0.7 V vs. RHE; Absolute values of the corresponding peak intensities from (C) Fig. 7A and (D) Fig. 7B as a function of time.

potential. As can be seen in Fig. S8A, a steady state was reached after 20 s when the potential -0.3 or -0.4 V was applied; however, at -0.5 and -0.6 V, the steady state was reached after 45 s. This kinetic delay might be due to the change in the species populating the surface of the CoNDs and the heightened production of formate ions at -0.5 and -0.6 V. On the other hand, at -0.7 V, the curve did not follow the same trend; it did not reach a steady state production for formate ions. This could be the result of exceeding the cathodic potential window at which the CO<sub>2</sub>RR took place on the surface of the CoNDs electrode. These observations agree with the results obtained from the potential-dependant in situ experiments at which maximum production of formate ions in the thin layer solution was determined to occur at -0.5 V. Fig. S8B showed a different trend for the peak intensities of  $\nu_3(CO_3^{2-})$  as a function of time. There was a nearly linear increase in intensity of  $\nu_3(CO_3^{2-})$  as the reaction progressed at -0.7 V rather than an initial increase followed by a much slower rise in intensity as observed for the reduction reactions at -0.3 and -0.4 V. For curves at -0.5 and -0.6 V, the rate of  $\nu_3(CO_3^{2-})$  production seemed to be close to those at

-0.3 and -0.4 V up to 55 s. After the 55 s, there was a faster increase in  $\nu_3(CO_3^{2-})$  production at -0.5 and -0.6 V relative to at -0.3 and -0.4 V. These results further strengthened the conclusion that the formation of carbonate ions depended on the applied potential.

### 3.5. CO<sub>2</sub> reduction reaction mechanism

Numerous literature reports have been exploring the possible mechanisms of the electrochemical CO<sub>2</sub>RR using Co-based catalysts theoretically and experimentally [24–27,56–61]. Most mechanisms were based on Tafel plots or DFT calculations. Here, in situ electrochemical FTIR spectroscopy was used to directly elucidate the possible reaction pathways of CO<sub>2</sub> reduction to formate on the surface of the CoNDs as illustrated in Scheme 2. First, CO<sub>2</sub> molecule approaches the catalyst surface close enough to gain an electron from the surface and form the adsorbed  $*COO^-$  intermediate. It has been shown through DFT calculations that this electron transfer and binding step of CO<sub>2</sub> to the surface is the rate-determining step [50,62,63]. Based on the surface



**Scheme 2.** Proposed mechanisms of the CO<sub>2</sub> reduction to formate on the surface of the CoND catalyst.

selection rule, Han et al. attributed the absence of  $\nu_{\text{as}}(^*\text{COO}^-)$  band in the IR spectra to the chemisorption of the carboxylate species on the electrode surface through the two oxygen atoms of the  $\text{COO}^-$  group symmetrically [64]. In the present study, it was determined that the  $^*\text{COO}^-$  intermediate was most likely adsorbed to the surface through the carbon (monodentate) rather than the two oxygen atoms (bidentate) since the  $\nu_{\text{as}}(^*\text{COO}^-)$  band was observed in the spectra. Moreover, the peak-fitting analysis of the high-resolution Co 2p<sub>3/2</sub> spectrum revealed that the CoND surface was made of 63% Co(OH)<sub>2</sub> and 37% Co<sub>3</sub>O<sub>4</sub>. Considering the surface composition and the negative potential applied to the electrode during the CO<sub>2</sub>RR, the  $^*\text{COO}^-$  intermediate was likely to initially bind to the surface through the carbon atom rather than the two oxygen atoms. Several theoretical and experimental studies have shown that formate production on metallic surfaces (e.g., Au, Ag, Cu, Ni, Pt and Sn) proceeds through a bidentate oxygen-bound intermediate, while the carbon-bound intermediate leads to CO production and further reduced C<sub>1</sub> products [44,50,65–68]. Chernyshova et al. employed *operando* surface-enhanced Raman scattering (SERS) combined with Tafel analysis and DFT simulations to decipher the possible intermediates during the conversion of CO<sub>2</sub> to formate on Cu(111) surface [69]. They found that both oxygen- and carbon-bound carboxylate intermediates could lead to the formate production. However, when the cathodic potential increased, the Cu-C bond weakened while the Cu-O bond stabilized, freeing the carbon atom to a second electron transfer reaction and to be protonated by a nearby adsorbed hydrogen atom [69]. In the *in situ* FTIR results presented in this study, it was evident that the  $^*\text{COO}^-$  intermediate was stable in the potential window of  $-0.1$  to  $-0.5$  V vs. RHE, as  $\nu_{\text{as}}(^*\text{COO}^-)$  band increased in intensity. In the potential window  $-0.6$  V to  $-0.8$  V, the  $\nu_{\text{as}}(^*\text{COO}^-)$  band decreased. This might be the result of weakened C-CoO<sub>x</sub> bond and the availability of the active site for HER. The second step of the reduction mechanism involved another electron transfer from the surface along with a proton transfer from solution to produce the formate ion. Due to similarities in the peak evolutions of  $\nu_3(\text{CO}_3^{2-})$  and  $\nu_{\text{as}}(^*\text{COO}^-)$  bands in the time-dependant SNIPTIR spectra prior to  $-0.5$  V, it was concluded that the carbonate ion production was linked to the production of the adsorbed intermediate. The dependence of the CO<sub>2</sub>RR current density on the concentration of bicarbonate ions was also observed by Zhang et al. using SnO<sub>2</sub> nanocrystals [70]. Thus, the bicarbonate ions in solutions might serve as a proton-donor to produce formate ions as illustrated in Scheme 2.

#### 4. Conclusions

In summary, we have demonstrated a facile approach for the direct

growth of CoNDs on a Co substrate without any surfactants and capping agents. The process is environment-friendly and can be easily scaled up for the large-scale preparation of the nanodendrites. The formed CoNDs exhibited a large EASA, high stability and superb enhanced catalytic activity for the selective electrochemical reduction of CO<sub>2</sub> to formate. NMR spectroscopy was employed to identify and quantify the products; and the COD was used to determine the Faraday efficiency. The effect of applied cathodic potential on the electrochemical reduction of CO<sub>2</sub> was also investigated, showing that the optimum electrode potential was in the range of  $-0.4$  to  $-0.5$  V vs. RHE, where the highest current efficiency was achieved. *In situ* electrochemical FTIR spectroscopy was further employed to investigate the mechanism and to monitor the kinetics of the electrochemical reduction of CO<sub>2</sub> at the CoNDs, providing molecular-level structural information about the intermediates and products. It was observed that the production of formate proceeded through the formation of a carbon-bound adsorbed  $^*\text{COO}^-$  intermediate. It was also found that the  $\text{HCO}_3^-$  -  $\text{CO}_3^{2-}$  equilibria played an important role in the formation of formate ion. The approach described in the present study open a door for the design of high-performance 3D nanostructured catalysts for energy and environmental applications.

#### CRediT authorship contribution statement

**Sharon Abner:** Conceptualization, Methodology, Investigation, Formal analysis, Writing – original draft. **Aicheng Chen:** Conceptualization, Supervision, Writing – review & editing, Funding acquisition.

#### Declaration of Competing Interest

The authors declare that they have no known competing financial interests or personal relationships that could have appeared to influence the work reported in this paper.

#### Acknowledgments

This work was supported by a Discovery grant from the Natural Sciences and Engineering Research Council of Canada (NSERC RGPIN-06248). A.C. acknowledges NSERC and the Canada Foundation for Innovation (CFI) for the Canada Research Chair Award in Electrochemistry and Nanoscience.

#### Appendix A. Supporting information

Supplementary data associated with this article can be found in the online version at doi:10.1016/j.apcatb.2021.120761.

#### References

- [1] G. Wang, J. Chen, Y. Ding, P. Cai, L. Yi, Electrocatalysis for CO<sub>2</sub> conversion: from fundamentals to value-added products, *Chem. Soc. Rev.* 50 (2021) 4993–5061, <https://doi.org/10.1039/D0CS00071J>.
- [2] M.G. Kibria, J.P. Edwards, C.M. Gabardo, C.T. Dinh, A. Seifitokaldani, D. Sinton, E. H. Sargent, Electrochemical CO<sub>2</sub> reduction into chemical feedstocks: from mechanistic electrocatalysis models to system design, *Adv. Mater.* 31 (2019) 1–24, <https://doi.org/10.1002/adma.201807166>.
- [3] A. Mustafa, B.G. Lougou, Y. Shuai, Z. Wang, S. Razzaq, E. Shagdar, J. Zhao, J. Shan, Recent progresses in the mechanism, performance, and fabrication methods of metal-derived nanomaterials for efficient electrochemical CO<sub>2</sub> reduction, *J. Mater. Chem. A* 9 (2021) 4558–4588, <https://doi.org/10.1039/d0ta11111b>.
- [4] D. Wu, G. Huo, W.Y. Chen, X.Z. Fu, J.L. Luo, Boosting formate production at high current density from CO<sub>2</sub> electroreduction on defect-rich hierarchical mesoporous Bi/Bi<sub>2</sub>O<sub>3</sub> junction nanosheets, *Appl. Catal. B: Environ.* 271 (2020), 118957, <https://doi.org/10.1016/j.apcatb.2020.118957>.
- [5] X. Wang, Y. Pan, H. Ning, H. Wang, D. Guo, W. Wang, Z. Yang, Q. Zhao, B. Zhang, L. Zheng, J. Zhang, M. Wu, Hierarchically micro- and meso-porous Fe-N4O-doped carbon as robust electrocatalyst for CO<sub>2</sub> reduction, *Appl. Catal. B: Environ.* 266 (2020), 118630, <https://doi.org/10.1016/j.apcatb.2020.118630>.
- [6] F. Zhang, C. Chen, S. Yan, J. Zhong, B. Zhang, Z. Cheng, Cu@Bi nanocone induced efficient reduction of CO<sub>2</sub> to formate with high current density, *Appl. Catal. A: Gen.* 598 (2020), 117545, <https://doi.org/10.1016/j.apcata.2020.117545>.

- [7] Z. Yin, G.T.R. Palmore, S. Sun, Electrochemical reduction of CO<sub>2</sub> catalyzed by metal nanocatalysts, *Trends Chem.* 1 (2019) 739–750, <https://doi.org/10.1016/j.trechm.2019.05.004>.
- [8] F. Yu, P. Wei, Y. Yang, Y. Chen, L. Guo, Z. Peng, Material design at nano and atomic scale for electrocatalytic CO<sub>2</sub> reduction, *Nano Mater. Sci.* 1 (2019) 60–69, <https://doi.org/10.1016/j.nanoms.2019.03.006>.
- [9] M.N. Hossain, Z. Liu, J. Wen, A. Chen, Enhanced catalytic activity of nanoporous Au for the efficient electrochemical reduction of carbon dioxide, *Appl. Catal. B Environ.* 236 (2018) 483–489, <https://doi.org/10.1016/j.apcatb.2018.05.053>.
- [10] M.N. Hossain, J. Wen, S.K. Konda, M. Govindhan, A. Chen, Electrochemical and FTIR spectroscopic study of CO<sub>2</sub> reduction at a nanostructured Cu/reduced graphene oxide thin film, *Electrochem. Commun.* 82 (2017) 16–20, <https://doi.org/10.1016/j.elecom.2017.07.006>.
- [11] M. Nur Hossain, S. Chen, A. Chen, Thermal-assisted synthesis of unique Cu nanodendrites for the efficient electrochemical reduction of CO<sub>2</sub>, *Appl. Catal. B Environ.* 259 (2019), 118096, <https://doi.org/10.1016/j.apcatb.2019.118096>.
- [12] M.N. Hossain, J. Wen, A. Chen, Unique copper and reduced graphene oxide nanocomposite toward the efficient electrochemical reduction of carbon dioxide, *Sci. Rep.* 7 (2017) 3184, <https://doi.org/10.1038/s41598-017-03601-3>.
- [13] S. Chen, A. Chen, Electrochemical reduction of carbon dioxide on Au nanoparticles: an in situ FTIR study, *J. Phys. Chem. C* 123 (2019) 23898–23906, <https://doi.org/10.1021/acs.jpcc.9b04080>.
- [14] W. Ren, C. Zhao, Paths towards enhanced electrochemical CO<sub>2</sub> reduction, *Natl. Sci. Rev.* 7 (2020) 7–9, <https://doi.org/10.1093/nsr/nwz121>.
- [15] X. Zhi, Y. Jiao, Y. Zheng, A. Vasileff, S.Z. Qiao, Selectivity roadmap for electrochemical CO<sub>2</sub> reduction on copper-based alloy catalysts, *Nano Energy* 71 (2020), 104601, <https://doi.org/10.1016/j.nanoen.2020.104601>.
- [16] L. Fan, C. Xia, F. Yang, J. Wang, H. Wang, Y. Lu, Strategies in catalysts and electrolyzer design for electrochemical CO<sub>2</sub> reduction toward C<sub>2</sub><sup>+</sup> products, *Sci. Adv.* 6 (2020) 1–18, <https://doi.org/10.1126/sciadv.aay3111>.
- [17] S. Chen, S.S. Thind, A. Chen, Nanostructured materials for water splitting - state of the art and future needs: a mini-review, *Electrochem. Commun.* 63 (2016) 10–17, <https://doi.org/10.1016/j.elecom.2015.12.003>.
- [18] Y. Li, Y. Sun, Y. Qin, W. Zhang, L. Wang, M. Luo, H. Yang, S. Guo, Recent advances on water-splitting electrocatalysis mediated by noble-metal-based nanostructured materials, *Adv. Energy Mater.* 10 (2020) 1–20, <https://doi.org/10.1002/aenm.201903120>.
- [19] C. Xi, C. Zou, M. Wang, D. Wu, H. Liu, C. Dong, X.W. Du, A bond-energy-integrated-based descriptor for high-throughput screening of transition metal catalysts, *J. Phys. Chem. C* 124 (2020) 5241–5247, <https://doi.org/10.1021/acs.jpcc.9b11902>.
- [20] M. Zhang, X. Li, J. Zhao, X. Han, C. Zhong, W. Hu, Y. Deng, Surface/interface engineering of noble-metals and transition metal-based compounds for electrocatalytic applications, *J. Mater. Sci. Technol.* 38 (2020) 221–236, <https://doi.org/10.1016/j.jmst.2019.07.040>.
- [21] M.Y. Lee, K.T. Park, W. Lee, H. Lim, Y. Kwon, S. Kang, Current achievements and the future direction of electrochemical CO<sub>2</sub> reduction: A short review, *Crit. Rev. Environ. Sci. Technol.* 50 (2020) 769–815, <https://doi.org/10.1080/10643389.2019.1631991>.
- [22] J. Wang, W. Cui, Q. Liu, Z. Xing, A.M. Asiri, X. Sun, Recent progress in cobalt-based heterogeneous catalysts for electrochemical water splitting, *Adv. Mater.* 28 (2016) 215–230, <https://doi.org/10.1002/adma.201502696>.
- [23] J. Cirone, S.R. Ahmed, P.C. Wood, A. Chen, Green synthesis and electrochemical study of cobalt/graphene quantum dots for efficient water splitting, *J. Phys. Chem. C* 123 (2019) 9183–9191, <https://doi.org/10.1021/acs.jpcc.9b00951>.
- [24] S. Gao, Y. Lin, X. Jiao, Y. Sun, Q. Luo, W. Zhang, D. Li, J. Yang, Y. Xie, Partially oxidized atomic cobalt layers for carbon dioxide electroreduction to liquid fuel, *Nature* 529 (2016) 68–71, <https://doi.org/10.1038/nature16455>.
- [25] S. Gao, X. Jiao, Z. Sun, W. Zhang, Y. Sun, C. Wang, Q. Hu, X. Zu, F. Yang, S. Yang, L. Liang, J. Wu, Y. Xie, Ultrathin Co<sub>3</sub>O<sub>4</sub> layers realizing optimized CO<sub>2</sub> electroreduction to formate, *Angew. Chem. - Int. Ed.* 55 (2016) 698–702, <https://doi.org/10.1002/anie.201509800>.
- [26] A. Aljabour, H. Coskun, D.H. Apaydin, F. Ozel, A.W. Hassel, P. Stadler, N. S. Sariciftci, M. Kus, Nanofibrous cobalt oxide for electrocatalysis of CO<sub>2</sub> reduction to carbon monoxide and formate in an acetonitrile-water electrolyte solution, *Appl. Catal. B Environ.* 229 (2018) 163–170, <https://doi.org/10.1016/j.apcatb.2018.02.017>.
- [27] P. Sekar, L. Calvillo, C. Tubaro, M. Baron, A. Pokle, F. Carraro, A. Martucci, S. Agnoli, Cobalt spinel nanocubes on N-doped graphene: a synergistic hybrid electrocatalyst for the highly selective reduction of carbon dioxide to formic acid, *ACS Catal.* 7 (2017) 7695–7703, <https://doi.org/10.1021/acscatal.7b02166>.
- [28] Z. Chen, G. Zhang, L. Du, Y. Zheng, L. Sun, S. Sun, Nanostructured cobalt-based electrocatalysts for CO<sub>2</sub> reduction: Recent progress, challenges, and perspectives, *Small* 16 (2020) 1–32, <https://doi.org/10.1002/sml.202004158>.
- [29] W. Ni, Z. Liu, X. Guo, Y. Zhang, C. Ma, Y. Deng, S. Zhang, Dual single-cobalt atom-based carbon electrocatalysts for efficient CO<sub>2</sub>-to-syngas conversion with industrial current densities, *Appl. Catal. B Environ.* 291 (2021), 120092, <https://doi.org/10.1016/j.apcatb.2021.120092>.
- [30] H. Yang, X. Wang, Q. Hu, X. Chai, X. Ren, Q. Zhang, J. Liu, C. He, Exosomes in tumor immunotherapy: mediator, drug carrier, and prognostic biomarker, *Adv. Biosyst.* 4 (2020), 2000061, <https://doi.org/10.1002/smbd.201900826>.
- [31] Y. Zhu, H. Zheng, Q. Yang, A. Pan, Z. Yang, Y. Qian, Growth of dendritic cobalt nanocrystals at room temperature, *J. Cryst. Growth* 260 (2004) 427–434, <https://doi.org/10.1016/j.jcrysgro.2003.08.037>.
- [32] X. Wang, G. Shi, F.N. Shi, G. Xu, Y. Qi, D. Li, Z. Zhang, Y. Zhang, H. You, Synthesis of hierarchical cobalt dendrites based on nanoflake self-assembly and their microwave absorption properties, *RSC Adv.* 6 (2016) 40844–40853, <https://doi.org/10.1039/c6ra06112e>.
- [33] Y. Zhang, S.X. Guo, X. Zhang, A.M. Bond, J. Zhang, Fine sediment and flow velocity impact bacterial community and functional profile more than nutrient enrichment, *Ecol. Appl.: a Publ. Ecol. Soc. Am.* 31 (2021) 02212, <https://doi.org/10.1016/j.nantod.2019.100835>.
- [34] J.Y. Ye, Y.X. Jiang, T. Sheng, S.G. Sun, In-situ FTIR spectroscopic studies of electrocatalytic reactions and processes, *Nano Energy* 29 (2016) 414–427, <https://doi.org/10.1016/j.nanoen.2016.06.023>.
- [35] L. Jin, A. Seifitokaldani, In situ spectroscopic methods for electrocatalytic CO<sub>2</sub> reduction, *Catalysts* 10 (2020) 481, <https://doi.org/10.3390/catal10050481>.
- [36] S.R. Chung, K.W. Wang, S.R. Sheen, C.T. Yeh, T.P. Perng, Electrochemical reduction and hydrogenation of Co oxides, *Electrochem. Solid-State Lett.* 10 (2007) A155–A158, <https://doi.org/10.1149/1.2730721>.
- [37] M.T. Makhlof, B.M. Abu-Zied, T.H. Mansour, Direct fabrication of cobalt oxide nanoparticles employing sucrose as a combustion fuel, *Phys. Chem. C* 2 (2013) 86–93, <https://doi.org/10.5923/j.pc.20120206.01>.
- [38] M.C. Biesinger, B.P. Payne, A.P. Grosvenor, L.W.M. Lau, A.R. Gerson, R.S.C. Smart, Resolving surface chemical states in XPS analysis of first row transition metals, oxides and hydroxides: Cr, Mn, Fe, Co and Ni, *Appl. Surf. Sci.* 257 (2011) 2717–2730, <https://doi.org/10.1016/j.apsusc.2010.10.051>.
- [39] C. He, Y. Zhang, Y. Zhang, L. Zhao, L.P. Yuan, J. Zhang, J. Ma, J.S. Hu, Molecular evidence for metallic cobalt boosting CO<sub>2</sub> electroreduction on pyridinic nitrogen, *Angew. Chem. - Int. Ed.* 59 (2020) 4914–4919, <https://doi.org/10.1002/anie.201916520>.
- [40] Y. Han, S. Axnanda, E.J. Crumlin, R. Chang, B. Mao, Z. Hussain, P.N. Ross, Y. Li, Z. Liu, Observing the electrochemical oxidation of Co metal at the solid/liquid interface using ambient pressure X-ray photoelectron spectroscopy, *J. Phys. Chem. B* 122 (2018) 666–671, <https://doi.org/10.1021/acs.jpcc.7b05982>.
- [41] N.R. Babji, E.O. McCusker, G.T. Whiteker, B. Canturk, N. Choy, L.C. Creemer, C.V.D. Amicis, N.M. Hewlett, P.L. Johnson, J.A. Knobelsdorf, F. Li, B.A. Lorschach, B. M. Nugent, S.J. Ryan, M.R. Smith, Q. Yang, NMR chemical shifts of trace impurities: industrially preferred solvents used in process and green chemistry, *Org. Process Res. Dev.* 20 (2016) 661–667, <https://doi.org/10.1021/acs.oprd.5b00417>.
- [42] K.P. Kuhl, E.R. Cave, D.N. Abram, T.F. Jaramillo, New insights into the electrochemical reduction of carbon dioxide on metallic copper surfaces, *Energy Environ. Sci.* 5 (2012) 7050–7059, <https://doi.org/10.1039/c2ee21234j>.
- [43] J.J. Max, C. Chapados, Isotope effects in liquid water by infrared spectroscopy. III. H<sub>2</sub>O and D<sub>2</sub>O spectra from 6000 to 10 cm<sup>-1</sup>, *J. Chem. Phys.* 131 (2009), 184505, <https://doi.org/10.1063/1.3258646>.
- [44] N.J. Firet, W.A. Smith, Probing the reaction mechanism of CO<sub>2</sub> electroreduction over Ag films via operando infrared spectroscopy, *ACS Catal.* 7 (2017) 606–612, <https://doi.org/10.1021/acscatal.6b02382>.
- [45] L. Lukashuk, N. Yigit, R. Rameshan, E. Kolar, D. Teschner, M. Hävecker, A. Knop-Gericke, R. Schlögl, K. Föttinger, G. Rupprecht, Operando insights into CO oxidation on cobalt oxide catalysts by NAP-XPS, FTIR, and XRD, *ACS Catal.* 8 (2018) 8630–8641, <https://doi.org/10.1021/acscatal.8b01237>.
- [46] M. Papasizaa, A. Cuesta, In situ monitoring using ATR-SEIRAS of the electrocatalytic reduction of CO<sub>2</sub> on Au in an ionic liquid/water mixture, *ACS Catal.* 8 (2018) 6345–6352, <https://doi.org/10.1021/acscatal.8b00977>.
- [47] C.M. Gunathunge, V.J. Ovalle, Y. Li, M.J. Janik, M.M. Waagele, Existence of an electrochemically inert CO population on Cu electrodes in alkaline pH, *ACS Catal.* 8 (2018) 7507–7516, <https://doi.org/10.1021/acscatal.8b01552>.
- [48] S. Xu, S. Chansai, Y. Shao, S. Xu, Y. Chi Wang, S. Haigh, Y. Mu, Y. Jiao, C.E. Stere, H. Chen, X. Fan, C. Hardacre, Mechanistic study of non-thermal plasma assisted CO<sub>2</sub> hydrogenation over Ru supported on MgAl layered double hydroxide, *Appl. Catal. B Environ.* 268 (2020), <https://doi.org/10.1016/j.apcatb.2020.118752>.
- [49] B. Innocent, D. Pasquier, F. Ropital, F. Hahn, J.M. Léger, K.B. Kokoh, FTIR spectroscopy study of the reduction of carbon dioxide on lead electrode in aqueous medium, *Appl. Catal. B Environ.* 94 (2010) 219–224, <https://doi.org/10.1016/j.apcatb.2009.10.027>.
- [50] Y. Katayama, F. Nattino, L. Giordano, J. Hwang, R.R. Rao, O. Andreussi, N. Marzari, Y. Shao-Horn, An in situ surface-enhanced infrared absorption spectroscopy study of electrochemical CO<sub>2</sub> reduction: selectivity dependence on surface C-bound and O-bound reaction intermediates, *J. Phys. Chem. C* 123 (2019) 5951–5963, <https://doi.org/10.1021/acs.jpcc.8b09598>.
- [51] S. Zhu, B. Jiang, W. Bin Cai, M. Shao, Direct observation on reaction intermediates and the role of bicarbonate anions in CO<sub>2</sub> electrochemical reduction reaction on Cu surfaces, *J. Am. Chem. Soc.* 139 (2017) 15664–15667, <https://doi.org/10.1021/jacs.7b10462>.
- [52] D. Shu, M. Wang, F. Tian, H. Zhang, C. Peng, A dual-cathode study on Ag-Cu sequential CO<sub>2</sub> electroreduction towards hydrocarbons, *J. CO<sub>2</sub> Util.* 45 (2021), 101444, <https://doi.org/10.1016/j.jcou.2021.101444>.
- [53] T. Tanaka, Y. Kameshima, S. Nishimoto, M. Miyake, Determination of carbonate ion contents in layered double hydroxides by FTIR spectrometry, *Anal. Methods* 4 (2012) 3925–3927, <https://doi.org/10.1039/c2ay25850a>.
- [54] B.G. Oliver, A.R. Davis, Vibrational spectroscopic studies of aqueous alkali metal bicarbonate and carbonate solutions, *Can. J. Chem.* 51 (1973) 698–702, <https://doi.org/10.1139/v73-106>.
- [55] G. Marcandalli, M. Villalba, M.T.M. Koper, The importance of acid–base equilibria in bicarbonate electrolytes for CO<sub>2</sub> electrochemical reduction and CO reoxidation studied on Au(hkl) electrodes, *Langmuir* 37 (2021) 5707–5716, <https://doi.org/10.1021/acs.langmuir.1c00703>.

- [56] R.E. Owen, J.P. O'Byrne, D. Mattia, P. Plucinski, S.I. Pascu, M.D. Jones, Cobalt catalysts for the conversion of CO<sub>2</sub> to light hydrocarbons at atmospheric pressure, *Chem. Commun.* 49 (2013) 11683–11685, <https://doi.org/10.1039/c3cc46791k>.
- [57] F. Borji, A.N. Pour, J. Karimi, M. Izadyar, Z. Keyvanloo, M. Hashemian, The molecular adsorption of carbon monoxide on cobalt surfaces: a DFT study, *Prog. React. Kinet. Mech.* 42 (2017) 89–98, <https://doi.org/10.3184/146867816X14799161258479>.
- [58] S. Gao, Z. Sun, W. Liu, X. Jiao, X. Zu, Q. Hu, Y. Sun, T. Yao, W. Zhang, S. Wei, Y. Xie, Atomic layer confined vacancies for atomic-level insights into carbon dioxide electroreduction, *Nat. Commun.* 8 (2017) 1–9, <https://doi.org/10.1038/ncomms14503>.
- [59] L. Wang, L. Wang, J. Zhang, X. Liu, H. Wang, W. Zhang, Q. Yang, J. Ma, X. Dong, S. J. Yoo, J.G. Kim, X. Meng, F.S. Xiao, Selective hydrogenation of CO<sub>2</sub> to ethanol over cobalt catalysts, *Angew. Chem. - Int. Ed.* 57 (2018) 6104–6108, <https://doi.org/10.1002/anie.201800729>.
- [60] S. Zhu, T. Li, W. Bin Cai, M. Shao, CO<sub>2</sub> electrochemical reduction as probed through infrared spectroscopy, *ACS Energy Lett.* 4 (2019) 682–689, <https://doi.org/10.1021/acsenergylett.8b02525>.
- [61] C. Zhu, Q. Wang, C. Wu, Rapid and scalable synthesis of bismuth dendrites on copper mesh as a high-performance cathode for electroreduction of CO<sub>2</sub> to formate, *J. CO<sub>2</sub> Util.* 36 (2020) 96–104, <https://doi.org/10.1016/j.jcou.2019.11.017>.
- [62] A.A. Peterson, J.K. Nørskov, Activity descriptors for CO<sub>2</sub> electroreduction to methane on transition-metal catalysts, *J. Phys. Chem. Lett.* 3 (2012) 251–258, <https://doi.org/10.1021/jz201461p>.
- [63] T. Tsujiguchi, Y. Kawabe, S. Jeong, T. Ohto, S. Kukunuri, H. Kuramochi, Y. Takahashi, T. Nishiuchi, H. Masuda, M. Wakisaka, K. Hu, G. Elumalai, J. Fujita, Y. Ito, Acceleration of electrochemical CO<sub>2</sub> reduction to formate at the Sn/reduced graphene oxide interface, *ACS Catal.* 11 (2021) 3310–3318, <https://doi.org/10.1021/acscatal.0c04887>.
- [64] C.H. Kim, S.W. Han, T.H. Ha, K. Kim, Self-assembly of anthraquinone-2-carboxylic acid on silver: Fourier transform infrared spectroscopy, ellipsometry, quartz crystal microbalance, and atomic force microscopy study, *Langmuir* 14 (1998) 6113–6120, <https://doi.org/10.1021/la981397b>.
- [65] X. Zhi, A. Vasilieff, Y. Zheng, Y. Jiao, S.Z. Qiao, Role of oxygen-bound reaction intermediates in selective electrochemical CO<sub>2</sub> reduction, *Energy Environ. Sci.* 14 (2021) 3912–3930, <https://doi.org/10.1039/d1ee00740h>.
- [66] J.T. Feaster, C. Shi, E.R. Cave, T. Hatsukade, D.N. Abram, K.P. Kuhl, C. Hahn, J. K. Nørskov, T.F. Jaramillo, Understanding selectivity for the electrochemical reduction of carbon dioxide to formic acid and carbon monoxide on metal electrodes, *ACS Catal.* 7 (2017) 4822–4827, <https://doi.org/10.1021/acscatal.7b00687>.
- [67] R. Kortlever, J. Shen, K.J.P. Schouten, F. Calle-Vallejo, M.T.M. Koper, Catalysts and reaction pathways for the electrochemical reduction of carbon dioxide, *J. Phys. Chem. Lett.* 6 (2015) 4073–4082, <https://doi.org/10.1021/acs.jpclett.5b01559>.
- [68] Z. Sun, T. Ma, H. Tao, Q. Fan, B. Han, Fundamentals and challenges of electrochemical CO<sub>2</sub> reduction using two-dimensional materials, *Chem* 3 (2017) 560–587, <https://doi.org/10.1016/j.chempr.2017.09.009>.
- [69] I.V. Chernyshova, P. Somasundaran, S. Ponnurangam, On the origin of the elusive first intermediate of CO<sub>2</sub> electroreduction, *Proc. Natl. Acad. Sci. U. S. A.* 115 (2018) E9261–E9270, <https://doi.org/10.1073/pnas.1802256115>.
- [70] S. Zhang, P. Kang, T.J. Meyer, Nanostructured tin catalysts for selective electrochemical reduction of carbon dioxide to formate, *J. Am. Chem. Soc.* 136 (2014) 1734–1737, <https://doi.org/10.1021/ja4113885>.